Green Chemistry

PAPER

View Article Online
View Journal | View Issue

Cite this: *Green Chem.*, 2025, **27**, 11438

Carbon-encapsulated FeNi nanoparticles for efficient magnetically induced levulinic acid hydrogenation

Tatiana Zanette,[a] Adrián García-Zaragoza,[a] Jaime Mazarío,[b] Jordan Santiago Martinez,[a] Bruno Chaudret,[b] Christian Cerezo-Navarrete *[a] and Pascual Oña-Burgos *[a]

Received 25th July 2025,
Accepted 11th August 2025

DOI: 10.1039/d5gc03853g

rsc.li/greenchem

Developing robust and efficient catalysts for magnetic induction heating (MIH) offers a sustainable approach for biomass valorization under mild conditions. Herein, we report a green and scalable synthetic method to prepare FeNi-based magnetic nanoparticles (MagNPs), with different atomic compositions, encapsulated in N-doped graphitic carbon (**Fe_1Ni_x@N-G**), *via* single-step pyrolysis of glucose and urea. These bimetallic nanoparticles serve both as efficient heating agents and active catalysts. Among them, **$Fe_1Ni_{0.25}$@N-G** demonstrated excellent catalytic performance in the magnetically induced hydrogenation of levulinic acid (LA) in aqueous solution, achieving full conversion and complete selectivity to γ-valerolactone (GVL) under mild conditions (63 mT, 320 kHz, 2 kW). Furthermore, the reactivity of **$Fe_1Ni_{0.25}$@N-G** was tested in the magnetically induced hydrogenation of other biomass-derived substrates of interest, such as 5-hydroxymethylfurfural (HMF), levoglucosenone, and vanillin, showing good activity and selectivity in all cases under mild reaction conditions. Finally, the robust encapsulation of the FeNi NPs in N-doped graphitic carbon strongly improved the stability of the catalyst in aqueous media, enabling its reuse up to four times under acidic conditions (pH ~2), for LA hydrogenation, and up to eight times under neutral conditions, such as HMF.

Green foundation

This work advances green chemistry by developing FeNi-based catalysts on N-doped graphitic carbon from glucose graphitization through a low-cost one-step pyrolysis method. This material enables the magnetically induced hydrogenation of levulinic acid in water under mild conditions, without using organic solvents.

The key green chemistry achievement lies in attaining high yields in the hydrogenation of biomass-derived molecules in water, such as levulinic acid (100% yield to GVL) and/or HMF (91% yield to BHMF), using magnetic induction heating as an energy-efficient technology. Both synthesis and catalysis maximize the use of renewable feedstocks, atom economy, and energy efficiency, and avoid hazardous solvents (principles 1, 2, 5, 6, 7, and 9).

A greener development could be achieved by reducing metal leaching under acidic conditions, enhancing catalyst durability. This improvement would also enable the integration of this strategy into continuous flow systems to significantly increase productivity.

Introduction

The energetic efficiency of catalytic processes is one of the main concerns in developing cost-effective and environmentally friendly industrial alternatives to traditional petrochemical routes. Commonly, conventional heated systems based on thermal convection, conduction, and radiation, such as flame and resistance heating in conventional furnaces, present drawbacks, such as heat loss and heat transfer limitations. In this sense, magnetic induction heating (MIH) shows great potential as a viable substitute for traditional heating methods.[1,2] This novel technique is based on the ability of ferromagnetic and conductive materials, commonly known as magnetic nanoparticles (MagNPs), to release heat through hysteresis losses when exposed to an alternating magnetic field (AMF).[3–6] MIH has attracted significant attention as a non-contact method for heating chemical reactions, primarily due to its unique advantages, such as localized and selective heating, which greatly improve the heat transfer of the process. Furthermore, this

[a]*ITQ, Instituto de Tecnología Química, Universitat Politècnica de València (UPV), Av. de los Naranjos S/N, 46022 Valencia, Spain. E-mail: chcena@itq.upv.es, pasoabur@itq.upv.es*

[b]*LPCNO, Laboratoire de Physique et Chimie des Nano-Objets, UMR5215 INSA-CNRS UPS, Institut des Sciences appliquées, 135, Avenue de Rangueil, F-31077 Toulouse, France*

technique demonstrated a series of benefits, such as the ability to heat and cool rapidly, resulting in high energy efficiency.[7–9] As a result, induction heating presents a promising solution for incorporating chemical reactions into systems with intermittent energy production.[10] Furthermore, the high capacity of MIH to quickly reach elevated temperatures allows the system to exceed the boiling point of the solvent by forming a vapor layer around the MagNPs. Thus, the reaction can be conducted under milder conditions (pressure and temperature) compared to conventional heating technologies.[11,12] In this regard, some of us have recently determined the surface temperature (T_{surf}) of magnetically heated MagNPs ($Fe_{2.2}C$@Ru) in solution through a catalytic approach.[13] It was found that the T_{surf} is significantly higher than the local temperature (T_{local}) measured in solution, which explains the remarkable catalytic performance of MagNPs when magnetically heated. Nonetheless, early research has indicated that elevated magnetic field amplitudes in aqueous media reduce the catalytic activity of these MagNPs due to particle sintering, thereby shortening their lifespan.[14] To address this issue, our research group synthesized a new carbon-encapsulated MagNP catalyst (FeCo@Ni@C), which effectively hydrogenated a variety of biomass-derived oxygenated compounds (such as furfural, 5-hydroxymethylfurfural, and vanillin) in water, being the first reported example of magnetically induced catalysis in aqueous media.[15] The main drawback of the previous study lies in employing the organometallic approach to synthesize MagNPs. This complex synthetic approach requires expensive organometallic precursors, and typically requires handling under inert atmospheres due to their low stability in air and/or water.[16] Therefore, it becomes crucial to explore novel, simpler, and cost-effective synthetic strategies to produce MagNPs on a large scale while guaranteeing their stability under an AMF. In this context, a promising and previously unexplored approach involves the use of metal nitrates as precursors of the MagNPs, along with their encapsulation within graphitic carbon *via* the high-temperature pyrolysis of glucose. This low-cost and facile graphitization process has been extensively studied over the past century, beginning with the introductory work of Acheson in 1896,[17] who demonstrated that the incorporation of metal catalysts such as Fe, Co, or Ni can significantly reduce the graphitization temperature of carbon precursors (from >3000 °C to ~800 °C).[18] Since then, numerous studies have explored the use of Fe in combination with simple carbon sources, such as glucose or sucrose, due to Fe's abundance, low toxicity, and catalytic efficiency for promoting graphitization.[19] This approach enables the one-step synthesis of well-encapsulated MagNPs in a carbonaceous matrix derived from renewable biomass resources.[20,21] For instance, Niu *et al.* synthesized carbon-encapsulated Fe_3O_4 nanoparticles from glucose for the removal of organic water pollutants.[22] For the same purpose, in 2019, Defilippi and co-workers obtained Fe_3C NPs supported on carbon nanocomposites through the pyrolysis of a mixture of $Fe(acac)_3$ and different carbon sources, such as glucose, sucrose, and chitosan.[23] Other studies have reported the synthesis of MagNP-based materials using comparable methodologies, but without exploring catalytic applications. For example, Hunter *et al.* investigated the influence of different carbon sources, including glucose, on the formation of mesoporous graphitic materials using $Fe(NO_3)_2$.[24] Gyergyek *et al.* synthesized magnetic Fe_3O_4 nanoparticles *via* pyrolysis of glucose and citric acid-coated Fe precursors, merely suggesting potential uses in magnetic catalysis without conducting any catalytic test.[25] These examples confirm the feasibility of glucose-based graphitization strategies using simple iron salts. However, most of these works focused on material synthesis or environmental applications, and none explored the use of such materials in catalytic hydrogenation reactions under magnetic induction heating.

The hydrogenation of biomass materials is crucial in producing value-added chemicals for industrial applications, enhancing the transition towards a carbon-neutral society.[26–28] Among these, levulinic acid (LA) is a renewable biomass platform chemical derived from inexpensive and abundant plant-based carbohydrates, such as cellulose. Consequently, LA is considered one of the twelve key building blocks that can be produced through the biological or chemical conversion of sugars and is well-suited to generate economically important derivatives.[29,30] Among them, γ-valerolactone (GVL) is one of the most valuable products obtained from the hydrogenation and dehydration of LA.[31] Two distinct pathways can be considered for this transformation, depending on whether dehydration or hydrogenation occurs first. GVL is a naturally occurring, safe, and biodegradable substance mainly applied in the industry as a food and fuel additive, which can also be used as a green solvent for biomass processing.[32,33] Typical catalysts used for the hydrogenation of LA into GVL often consist of monometallic noble metal-based nanoparticles (Ru, Ir, Pd, Pt, *etc.*)[26,34–37] or even bimetallic nanoparticles (RuRe or RuSn)[38,39] supported over high surface area supports. However, the benchmark catalysts leading to the best yields for GVL production are based on carbon-supported Ru nanoparticles (Ru/C).[40–42] The major limitation of using this type of catalyst is the reliance on noble metals, which are costly and have natural scarcity. For this reason, the use of non-noble metal-based catalysts has attracted growing interest from the scientific community,[43–47] nickel (Ni) being one of the most active first-row transition metals for the hydrogenation of LA. For example, Komandur *et al.* have conducted the hydrogenation of LA in the gas phase using a Ni-hydroxyapatite-supported catalyst, achieving complete conversion and high selectivity (>90%) to GVL.[48] Another work by Yan and co-workers reported the use of a Ni/C catalyst, derived from MOF pyrolysis, to achieve GVL yields of 98% and 86% using dioxane and isopropanol as solvents, respectively.[49] Similarly, Liang *et al.* obtained a complete GVL yield using Ni nanoparticles over a porous carbon catalyst.[50] A common issue in the mentioned studies is the extreme reaction conditions, such as high temperatures (200 °C) and elevated H_2 pressures (10–35 bar). Focusing on milder reaction conditions, our research group has considered the use of MIH in the hydrogenation of LA, by using a core–shell catalyst based on FeCo@Ni NPs encapsu-

lated on carbon (FeCo@Ni@C). Concretely, after 20 hours of reaction and under mild reaction conditions (3 bar H_2, 110 °C, and inductor equipment of 5 kW), the catalyst achieved a low yield of 29% in the production of GVL, using water as solvent.[15] Similarly, Raya-Barón *et al*. reported the hydrogenation of LA using non-supported water-soluble Ni NPs, which exhibited a maximum yield of 65%, although without full selectivity toward GVL.[14] To the best of our knowledge, apart from these contributions, there is only one other report, by Gyergyek and coworkers, which employed MIH in the catalytic hydrogenation of LA, achieving complete conversion to GVL using a Ru-based nanoparticle composite over maghemite and isopropanol as solvent.[51]

Herein, we designed a series of multifunctional bimetallic FeNi-supported nanoparticles obtained through the graphitization of glucose (**Fe_xNi_y@N-G**) for the magnetically induced hydrogenation of LA in aqueous solution. The FeNi NPs are ferromagnetic, where iron acts as the heating agent and nickel as the catalytically active species in the hydrogenation reaction. In that sense, a clear trend was observed between the amount of nickel added and the catalytic activity of the FeNi-based catalyst, yielding remarkable results in catalytic activity and selectivity towards GVL. Furthermore, a range of high-interest biomass-derived substrates were also hydrogenated, demonstrating that the bimetallic **Fe_1Ni_x@N-G** catalysts are highly active in all cases. Finally, due to the efficient encapsulation of the MagNPs in the carbon matrix, the catalyst demonstrated stability during several catalytic cycles, without significant loss of activity.

Results and discussion

Synthesis and structural characterization

The synthesis of bimetallic FeNi NPs supported on layered N-doped graphite is based on the graphitization of glucose through a pyrolysis process. This synthetic approach has been used to design mono- and bimetallic FeNi NPs with different atomic compositions (see Fig. 1a). Specifically, $Fe(NO_3)_3{\cdot}9H_2O$ and $Ni(NO_3)_2{\cdot}6H_2O$ salts were used as metal precursors in different proportions, along with glucose and urea as carbon and nitrogen sources to obtain N-doped graphite (**N-G**). Briefly, all the reactants were dissolved in distilled water and transferred into a stainless-steel autoclave, which was sealed and heated for 18 h at 175 °C under dynamic conditions. Then, the preformed carbon-based materials were pyrolyzed (750 °C, 2 h, 25 °C min^{-1}), resulting in five different catalysts based on mono- and bimetallic FeNi NPs: **Fe@N-G**, **$Fe_1Ni_{0.05}$@N-G**, **$Fe_1Ni_{0.1}$@N-G**, **$Fe_1Ni_{0.25}$@N-G**, and **$Fe_1Ni_{0.4}$@N-G** (see SI section S1.2). The metal contents of the bimetallic carbon-based catalysts were determined by inductively coupled plasma optical emission spectroscopy (ICP-OES), showing a very similar Fe wt% content in all materials, differing only in the amount of Ni (see SI section S1, Table S1.1). Brunauer–Emmett–Teller (BET)[52] and Barret–Joyner–Halenda (BJH)[53] sorption analyses were performed to determine the specific surface area and porosity of the catalysts. All samples exhibited similar surface areas, ranging from 240 to 270 m^2 g^{-1}, with pore volumes around 0.1 cm^3 g^{-1} (see SI section S3, Table S3.1). These values indicate a relatively large active surface for this type of graphitic materials.

Transmission electron microscopy (TEM) analysis of FeNi-based catalysts revealed the formation of well-distributed nanoparticles with a mean size distribution that increases with the Ni loading. For example, **Fe@N-G** exhibited a size of 8.5 ± 3.1 nm, while **$Fe_1Ni_{0.4}$@N-G** presents an average diameter of 10.1 ± 4.5 nm (see Fig. 1). In all cases, the nanoparticles present a spherical morphology and are perfectly distributed over a homogeneous graphite layer, providing excellent stability to these systems (*vide infra*). The synthesis of carbon-based supported nanoparticles from the graphitization of glucose has been previously described, as we mentioned throughout the introduction. However, this approach has never been explored with the aim of synthesizing MagNPs for application in magnetically induced catalysis for biomass valorisation. Additionally, due to the inclusion of urea in the pyrolysis process, the obtained graphite layer is doped with N atoms, as confirmed by elemental analysis (see SI section S3, Table S3.1), which enhances the stability of the system by facilitating the interaction between the metal and the support.[54] This was corroborated by performing the same synthetic procedure without adding urea (**$Fe_1Ni_{0.25}$@G**). TEM images revealed that the undoped MagNPs were larger in size (22.4 ± 15.7 nm) and the nanoparticle dispersion was considerably poorer (Fig. 1g). This difference in size and dispersion indicates that the nitrogen atoms in the N-doped graphite support play an important role in facilitating the stabilization of the FeNi-based NPs in this synthetic approach.

The composition and crystalline structure of the different MagNPs were investigated by high-resolution TEM (HRTEM) and scanning transmission electron microscopy dark field (STEM-DF) coupled with energy-dispersive X-ray (EDX) spectroscopy. HRTEM micrographs of FeNi-based catalysts revealed the formation and crystallinity of the nanoparticles in all the magnetic catalysts synthesized. Notably, according to the obtained images, the MagNPs consist of a FeNi-alloy well-encapsulated in a carbon layer (Fig. 2a). HRTEM micrographs of **$Fe_1Ni_{0.25}$@N-G** indicated the existence of crystalline NPs mainly composed of two different crystalline structures, since two different lattice fringes can be observed. Specifically, in **$Fe_1Ni_{0.25}$@N-G**, lattice fringes with interplanar distances of 1.44 Å and 2.09 Å can be identified, which can be attributed to the (200) plane of the body centred-cubic (*bcc*) structure of Fe (*bcc*-Fe; JCPDS: 03-065-4899) and the (111) plane of the face-centred cubic (*fcc*) structure of alloy-FeNi (*fcc*-FeNi; JCPDS: 00-047-1417) (Fig. 2a and Fig. S4.1, see SI section S4). Furthermore, HRTEM images of **$Fe_1Ni_{0.25}$@N-G** showed that the MagNPs are well covered by a carbon layer of approximately 3 nm in thickness (Fig. 2b). By further analysis of this layer, a lattice spacing of 3.1 Å was estimated, close to the (002) plane of C_2N_2O.[55] This precise encapsulation of the FeNi NPs should protect them from sintering at the high temperatures reached

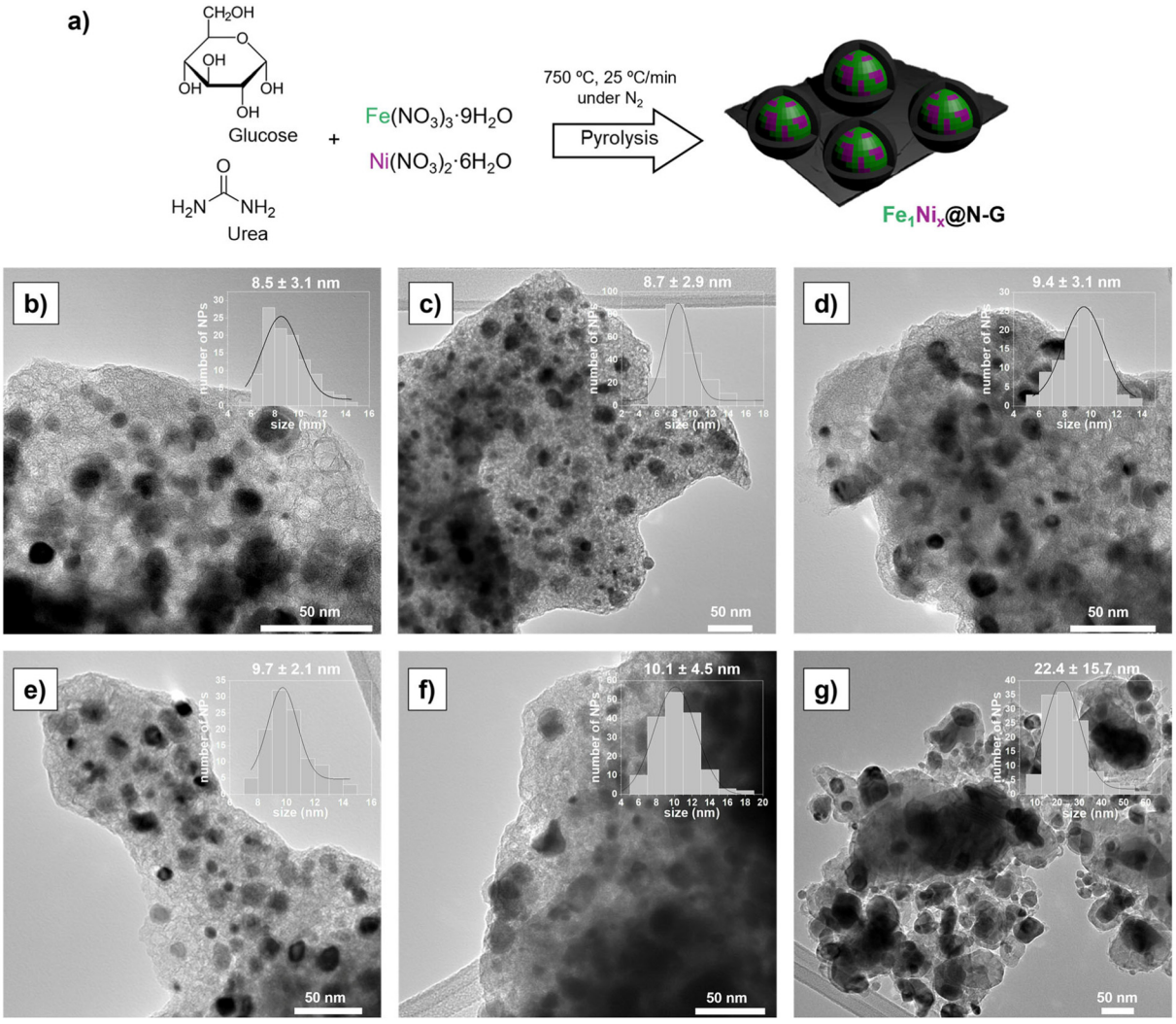

Fig. 1 (a) Synthesis of FeNi NPs supported on layered N-doped graphite (**Fe_1Ni_x@N-G**) with different atomic compositions. TEM micrographs and the corresponding size histograms of (b) **Fe@N-G**, (c) **$Fe_1Ni_{0.05}$@N-G**, (d) **$Fe_1Ni_{0.1}$@N-G**, (e) **$Fe_1Ni_{0.25}$@N-G**, (f) **$Fe_1Ni_{0.4}$@N-G**, and (g) **$Fe_1Ni_{0.25}$@G**.

during the magnetically induced catalysis (*vide infra*). The formation of the FeNi alloy has been confirmed by STEM-HAADF imaging coupled with EDX analysis. In particular, EDX elemental mapping and line scan profile of **$Fe_1Ni_{0.25}$@N-G** corroborate that both metals are present in an intimate mixture in the same nanoparticle, forming an FeNi alloy with an atomic composition of $Fe_1Ni_{0.26}$, which matches well with the ICP results (see SI section S1, Table S1.1).

X-ray powder diffraction (XRD) analysis also revealed the crystalline nature of the FeNi NPs in all the synthesized catalysts. Remarkably, the XRD pattern of the monometallic Fe NPs (**Fe@N-G**) differs significantly from their bimetallic counterparts. As shown in Fig. S5.1 (see SI section S5), the XRD of **Fe@N-G** exhibits peaks corresponding to *bcc*-Fe and θ-Fe_3C (JCPDS: 00-035-0772), suggesting that Fe undergoes a partial carburization during the graphitization of glucose (750 °C under N_2). In contrast, the FeNi-based catalysts do not exhibit peaks corresponding to Fe carburization, suggesting that Ni inhibits the carburization process during pyrolysis. Instead, the bimetallic FeNi-catalysts exhibit peaks at 2θ: ~43.8° and ~44.7° corresponding to *fcc*-FeNi and *bcc*-Fe, respectively, with a small peak at 2θ: 26.5° due to the N-doped carbon-coating formed during the graphitization process, corresponding to graphite (JCPDS: 03-065-6212; see Fig. 3a), as previously observed in the HRTEM analysis (Fig. 2b). No peaks related to oxidized species, such as Fe_3O_4 or NiO, can be observed, confirming that the bulk of the **Fe_1Ni_x@N-G** catalysts are fully reduced, which are the active species in the hydrogenation reactions (*vide infra*). As shown in Fig. 3a, as the amount of Ni increases, the peak intensity related to the *fcc*-FeNi also increases without a significant shift, while the peak corresponding to the *bcc*-Fe phase decreases. According to Vegard's law for solid solutions, the alloy-FeNi phase resulted in a stoichiometry of approximately Fe_1Ni_1 in all cases, regardless of the amount of nickel present in the sample (Fig. 3b). This suggests that while the overall nickel content in the system

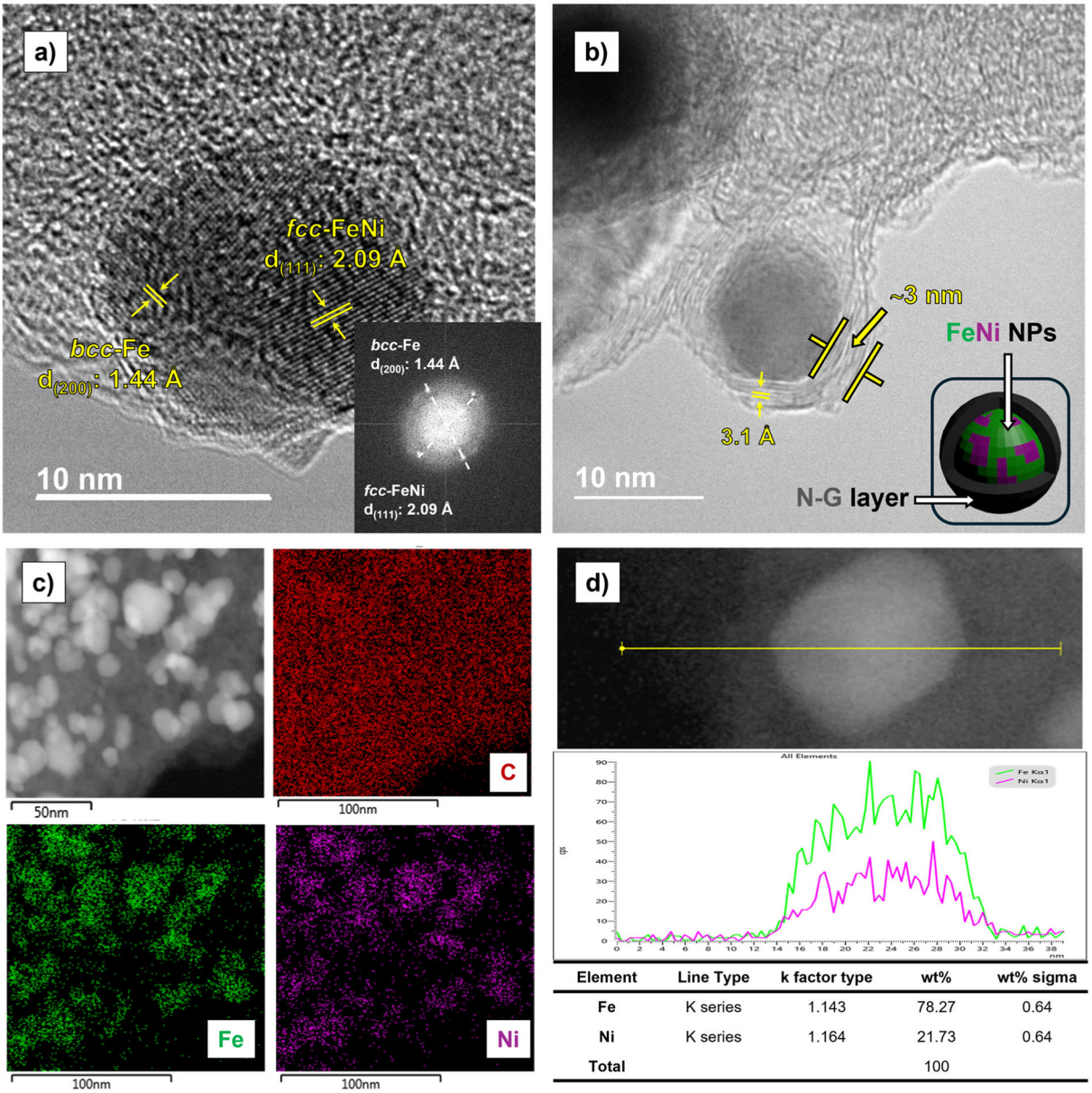

Element	Line Type	k factor type	wt%	wt% sigma
Fe	K series	1.143	78.27	0.64
Ni	K series	1.164	21.73	0.64
Total			100	

Fig. 2 (a) HRTEM image of **$Fe_1Ni_{0.25}$@N-G**, where FFT analysis confirms the presence of *fcc*-FeNi and *bcc*-Fe crystalline structures. (b) HRTEM image of **$Fe_1Ni_{0.25}$@N-G** highlighting the separation of the carbon layers (3.1 Å) and the thickness of the carbon coat (*ca.* 3 nm). (c) STEM-HAADF coupled with EDX analysis of **$Fe_1Ni_{0.25}$@N-G**, where C is marked in red, Fe in green, and Ni in violet. (d) STEM-HAADF image and EDX line scan profile of a single nanoparticle of **$Fe_1Ni_{0.25}$@N-G**.

increases, the proportion of the *fcc*-Fe_1Ni_1 phase grows, but its stoichiometry does not shift in favour of nickel. However, the full width at half maximum (FWHM) of the *fcc*-Fe_1Ni_1 signal varies depending on the amount of Ni added. Consistent with the observations from TEM micrographs (*vide supra*), the crystal size (calculated using the Scherrer equation) increases according to the Ni content of the system, with **$Fe_1Ni_{0.05}$@N-G** exhibiting the smallest crystal size and **$Fe_1Ni_{0.4}$@N-G** exhibiting the largest (see SI section S5, Table S5.1). Therefore, XRD measurements indicate that the FeNi-based catalysts are composed primarily of monometallic iron nanoparticles, which are progressively modified with small but increasing proportions of the alloyed Fe_1Ni_1 phase, which are ultimately encapsulated within a carbon shell.

XPS analysis confirmed the chemical composition of these N-doped graphite materials. Fig. 4 presents the XPS spectra of Fe(2p), Ni(2p), C(1s) and N(1s) regions in the mono- and bi-metallic catalysts (**Fe@N-G** and **$Fe_1Ni_{0.25}$@N-G**, respectively). Given that the presence of graphene/graphite layers was already confirmed by TEM and XRD, curve fitting of the C(1s) XP region (Fig. 4a) could be satisfactorily accomplished by using the model developed by J. Baltrusaitis and co-workers as

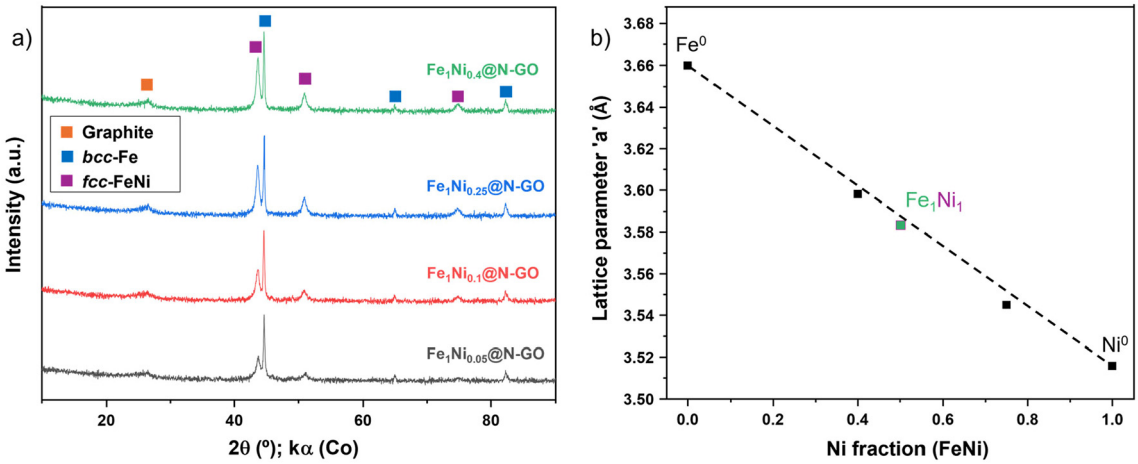

Fig. 3 (a) XRD diffractograms of **$Fe_1Ni_{0.05}$@N-G** (grey), **$Fe_1Ni_{0.1}$@N-G** (red), **$Fe_1Ni_{0.25}$@N-G** (blue), and **$Fe_1Ni_{0.4}$@N-G** (green). (b) Fitting of the lattice parameter of the fcc-FeNi alloy phase to a calibration curve generated from the lattice parameters of *fcc*-Fe^0, *fcc*-$Fe_1Ni_{0.4}$, *fcc*-$Fe_1Ni_{0.75}$ and *fcc*-Ni^0, demonstrating a resulting stoichiometry of *ca.* Fe_1Ni_1 for all synthesized-catalysts.

a starting point.[56] Both samples exhibit a high degree of similarity, with two main components at 284.8 eV, corresponding to C–C, C–H (sp^3), and 284.4 eV, corresponding to C=C (sp^2). The other peaks correspond to carbon atoms bound to O or N, such as C=N, C–N, and C–O (*ca.* 286.0 eV) and O–C=O (*ca.* 289.0 eV).[57,58] It is important to note that while the XRD analysis of **Fe@N-G** shows the presence of an iron carbide phase (θ-Fe_3C), the substantial quantity of other types of carbon on the sample surfaces makes it difficult to identify these species in the C(1s) region. The N(1s) regions of both systems (**Fe@N-G** and **$Fe_1Ni_{0.25}$@N-G**) are also very similar (Fig. 4b), showing spectra centred at 400 eV that can be fitted using three components. The main peak at *ca.* 400.3 eV can be ascribed to N atoms forming part of organic structures, but coordinated to metal (Fe, Ni) atoms, whereas the peak at *ca.* 401.3 eV might belong to isolated graphitic and/or pyrrolic nitrogen atoms, and the peak at *ca.* 398.2 eV can be assigned to pyridine and/or imine-like N atoms.[57,59,60] All these contributions point to the effective incorporation of the N atoms into the carbonaceous matrix, in agreement with HRTEM analyses, as well as to a stabilizing effect over the metal species. As for the metallic elements, the weak intensity of Fe(2p) and Ni (2p) regions (Fig. 4c and d) is due to the carbon encapsulation of the MagNPs, which led to a low response in the XPS spectrum. Due to the low signal-to-noise ratio and the presence of multiplet splitting in these regions, it was not possible to perform any fitting, and the discussion was based on the visual inspection of the spectra. Fig. 4c shows the Ni $2p_{3/2}$ and Ni $2p_{1/2}$ peaks (overlapped with an Auger feature from N) for **$Fe_1Ni_{0.25}$@N-G**, within a BE range of 845–890 eV. The Ni $2p_{3/2}$ peak maxima is located at *ca.* 854.2 eV, which can be associated with oxidized species. The apparent low intensity ratio between the expected satellite at *ca.* 862 eV and the main peak prompted us to tentatively associate these species with a nickel-based oxyhydroxide.[61] Additionally, an asymmetry on the low binding energy side of the peak indicates the presence of Ni(0) in the XPS analysis depth (*ca.* 852.6 eV).[61] Finally, the Fe(2p) XP region of **Fe@N-G** and **$Fe_1Ni_{0.25}$@N-G** samples present a shoulder at 706.8 eV in the Fe($2p_{3/2}$) region, characteristic of the iron metal. Apart from that component, in both XPS spectra, the maxima of the Fe(2p) XP peaks appear around 711.1 and 724.6 eV, suggesting oxidized iron as the predominant species.[62] Additionally, the area of the spectra between ~707 eV and ~710 eV (Fig. 4d), in both catalysts might contain minor contributions from Fe^{3+} in Fe_3C (708.1 eV) as well as Fe^{2+} in FeO (709.7 eV).[62,63] Comparing the Fe(2p) and Ni(2p) regions in the XP spectra (Fig. 4c and d), it is apparent that the Ni signal is more intense despite Fe being more abundant in the bulk. This observation supports a structural model in which Ni is preferentially located at the nanoparticle surface, consistent with partial shell or surface-decorated configurations around a Fe-rich core, resulting in what we describe as a "cookie-like" morphology (see SI section S6, Fig. S6.3).

The quality of the formed graphite layer can be confirmed by Raman spectroscopy.[64] In all cases, two major bands are observed: one at *ca.* 1358 cm^{-1} (D peak) and another at *ca.* 1584 cm^{-1} (G peak), along with a broad 2D peak around 3000 cm^{-1}, which is associated with 1–2 graphene layers. The number of defects in the N-G support is related to the intensities of the D and 2D bands, and these peaks are quite intense for all the materials obtained (see SI section S7, Fig. S7.1). These defects in the N-doped graphite are exceptional anchoring points for the FeNi nanoparticles,[65] enhancing the carbon–metal interaction, which may improve the activity and stability of the catalysts. However, vibrations associated with the interactions of carbon, oxygen or nitrogen atoms with the metallic nanoparticles (Fe and/or Ni) could not be observed.

Due to their application in magnetically induced catalysis, the characterization of the encapsulated FeNi NPs also included both magnetic and calorimetric measurements. Magnetic properties were analysed using vibrating sample magnetometry (VSM), measuring hysteresis cycles at 5 and

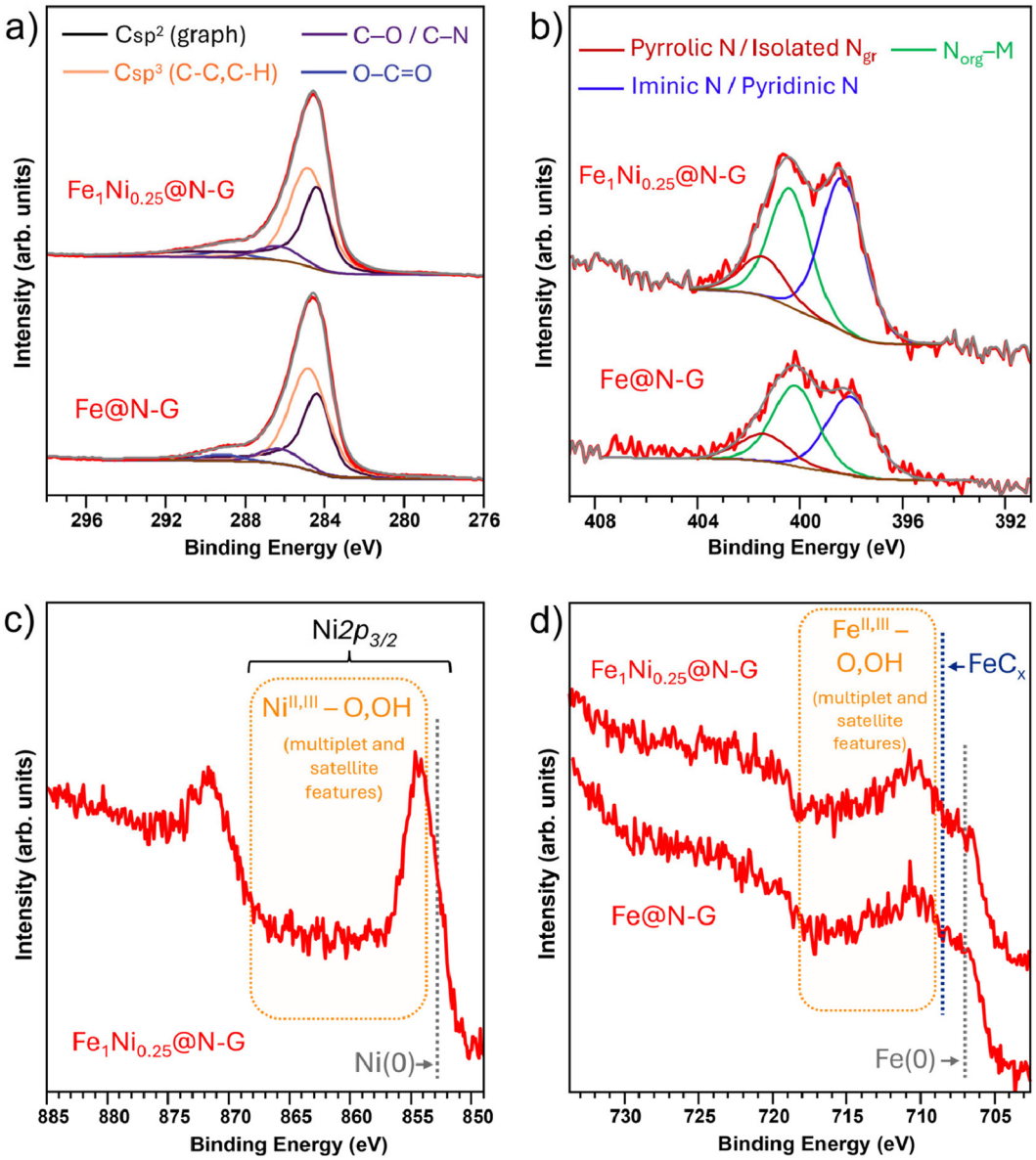

Fig. 4 XPS spectra of **Fe@N-G** and **$Fe_1Ni_{0.25}$@N-G**, including (a) C(1s), (b) N(1s), (c) Ni(2p), and (d) Fe(2p) regions.

300 K (see SI section S8, Fig. S8.1–S8.5) to determine the saturation magnetization (M_S), remanent magnetization (M_R), and the coercive field. From Table 1, at 300 K, the remanence ratios (M_R/M_S) are slightly above or below 0.1, indicating that the systems are ferromagnetic, but close to the boundary between superparamagnetic and ferromagnetic behaviour. As expected, M_R values become significantly higher at 5 K than at 300 K, where thermal fluctuations suppress magnetic stability at room temperature. Therefore, at 5 K, the remanence increases for all samples, indicating a transition into a blocked state where the nanoparticles behave as mono-domain ferromagnetic particles.[66] Interestingly, despite the lower magnetic moment per atom of Ni, M_s values generally increase with Ni incorporation, particularly at 300 K. It is likely that strong magnetic interactions stabilizing the *fcc*-FeNi alloy phase are behind this phenomenon.[67] However, other effects may also account for this circumstance, and the exploration of this lies beyond the scope of this work. On the other hand, the M_R

Table 1 Values of M_S, M_R and SAR of **Fe_1Ni_x@N-G** catalysts

Catalyst	M_S (A m² kg_{Co}^{-1}) 5 K	M_S (A m² kg_{Co}^{-1}) 300 K	M_R (A m² kg_{Co}^{-1}) 5 K	M_R (A m² kg_{Co}^{-1}) 300 K	SAR[a] (W g^{-1})
Fe@N-G	130	110	42	18	72
$Fe_1Ni_{0.05}$@N-G	152	124	34	10	24
$Fe_1Ni_{0.1}$@N-G	165	145	30	14	32
$Fe_1Ni_{0.25}$@N-G	169	131	32	9	50
$Fe_1Ni_{0.4}$@N-G	177	159	46	24	68

[a] SAR estimated with a 93 kHz coil operating at 47 mT.

decreases at first with Ni incorporation (*i.e.*, **$Fe_1Ni_{0.05}$@N-G**), to then increase again with higher amounts of Ni (*i.e.*, **$Fe_1Ni_{0.4}$@N-G**). Here, two effects are probably counteracting each other at the extremes of the compositional range studied. Fe would in principle enhance magnetic anisotropy, but the average particle size becomes larger (Fig. 1) when increasing the Ni content. Last, any significant exchange bias could be measured in the $\mu_0 H$ axis at 5 K, thus proving the absence of a significant layer of oxide at the NP surfaces.[68]

On the other hand, calorimetric characterization was conducted through specific absorption rate (SAR) measurements using an AMF at 93 kHz and 47 mT. SAR quantifies the heating efficiency of the nanoparticles (see SI section S1.1), which is crucial for any application involving their activation under an AMF. The SAR measurements (Table 1) reveal that **Fe@N-G** exhibits the highest SAR (72 W g^{-1}), as expected for a hard magnetic material with a higher efficiency in dissipating heat under an AMF. Although the SAR values of the FeNi alloy-based catalysts are lower than that of the monometallic Fe catalyst, a similar trend to what is observed in the values of M_R was detected within the alloy series. As the Ni content increases, the SAR first decreases (24 W g^{-1} for **$Fe_1Ni_{0.05}$@N-G**) to then increase (68 W g^{-1} for **$Fe_1Ni_{0.04}$@N-G**). Again, a complex interplay of changes in anisotropy, particle size distribution, and magnetic relaxation upon Ni incorporation should account for these results. Overall, these measurements highlight that these FeNi-based systems exhibit tuneable magnetic and heating properties, with Fe-rich compositions retaining better magnetization and heat dissipation performance.

Catalytic studies

The catalytic performances of **Fe@N-G**, **$Fe_1Ni_{0.05}$@N-G**, **$Fe_1Ni_{0.1}$@N-G**, **$Fe_1Ni_{0.25}$@N-G**, and **$Fe_1Ni_{0.4}$@N-G** have been studied during the magnetically induced hydrogenation of levulinic acid (LA) in water under 5 bar H_2. LA has been selected as a model molecule because its reduction to γ-valerolactone (GVL) is highly significant, as GVL is a compound of great interest as a potential substitute for petroleum-based fuels[33,69] and a promising green solvent.[70] However, most of the catalysts reported for GVL production from LA are water-incompatible, requiring the use of organic solvents. Since real biomass products dissolve primarily in water, which is considered the greenest solvent due to its nontoxicity and environmental compatibility,[71] it is crucial to design robust catalytic systems that operate in aqueous media. Therefore, we conducted the magnetically induced hydrogenation of LA in aqueous media under an AMF, which also poses an additional layer of complexity due to the commonly poor dispersability and limited stability of MagNPs in water.[13–15]

For the magnetically induced reactions, an AC magnetic field oscillating at 320 kHz with a maximum power of 2 kW was used (see SI section S2). Initially, the reaction conditions were optimized for the applied magnetic field, temperature, catalyst loading, and H_2 pressure, as shown in Table S9.1 and Fig. S9.1 (see SI section S9). Under the optimized reaction conditions (0.4 mmol LA, 30 mg of **Fe_1Ni_y@N-G** catalyst, 8 hours, 63 mT, and 5 bar H_2), the activity and selectivity of the different catalysts were compared. Regarding the monometallic catalyst, as shown in Table S9.1 entry 1, **Fe@N-G** exhibited no catalytic activity, confirming that Ni is the active species responsible for the hydrogenation of LA, while Fe serves merely as a crucial component of the heating agent. This observation aligns with literature reports, as Ni-based catalysts are widely used in the hydrogenation of biomass molecules due to their capacity to efficiently dissociate and chemisorb H_2.[72]

For the bimetallic catalyst, an increase in Ni-loading led to higher conversion rates. For example, after 4 h of reaction, chosen to avoid comparing catalyst performance at high conversion levels, the **$Fe_1Ni_{0.05}$@N-G** catalyst achieved only 17% conversion (Table S9.1, entry 2). In contrast, **$Fe_1Ni_{0.1}$@N-G** or **$Fe_1Ni_{0.25}$@N-G** showed significantly higher conversions of 46% and 63%, respectively, with **$Fe_1Ni_{0.4}$@N-G**, the catalyst with the highest Ni-content, achieving a maximum conversion of 92% (Table S9.1, entry 5). These results indicate that a higher number of catalytically active sites (Ni) improves the overall conversion in the magnetically induced hydrogenation of LA. Interestingly, the selectivity toward GVL remained consistent at 100% for all Ni loadings, with no intermediates or over-hydrogenated products detected.

Besides, a clear trend can be observed in the local temperature (T_{local}) reached by the catalyst under the influence of the oscillating magnetic field, which depends on the hard–soft magnetic nature and the loading of the ferromagnetic nanoparticles. As can be observed by comparing entries 1 to 5 in Table S9.1, the magnetic catalyst that achieves the highest T_{local} (measured using an IR pyrometer) is the monometallic Fe-based catalyst (**Fe@N-G**). This observation is in good agreement with the SAR measurements and expected since Fe is magnetically harder than Ni. Therefore, Fe tends to reach a higher T_{local} (151 °C). When Ni is incorporated into the magnetic catalysts, the measured T_{local} decreases compared to **Fe@N-G**. However, as the Ni content increases, the T_{local} gradually rises from 99 °C for **$Fe_1Ni_{0.05}$@N-G** to 146 °C for **$Fe_1Ni_{0.4}$@N-G**. This trend is consistent with the SAR measurements, where the SAR values initially decrease and then increase with the Ni content (see Table 1). Remarkably, even though none of the FeNi-based catalysts surpass the temperature reached by **Fe@N-G**, all of them are more active in the hydrogenation of LA. Therefore, this demonstrates that Ni is the active species responsible for the hydrogenation reaction.

Given that **$Fe_1Ni_{0.25}$@N-G** contains a moderate amount of Ni and exhibits a higher TOF value than **$Fe_1Ni_{0.4}$@N-G**, we further explored the correlation between the observed T_{local} and the performance of the catalyst under magnetic heating. To do that, the activation energy (Ea) of **$Fe_1Ni_{0.25}$@N-G** for the hydrogenation of LA was determined using the Arrhenius equation under conventional heating, assuming the same reaction mechanism under both conventional and magnetic heating. This allowed us to establish a correlation between conversion and temperature, enabling an estimation of the real surface temperature (T_{surf}) of the catalyst, as demonstrated

previously.[15] Plotting the apparent kinetic constant (k) for the hydrogenation of LA (**1**) to GVL (**3**) at different temperatures (ranging from 80 to 160 °C; see SI section S9, Fig. S9.2) results in an estimated Ea of 20.9 kJ mol^{-1} for **$Fe_1Ni_{0.25}$@N-G** (Fig. 5b). As shown in Fig. 5c, the conversion increased proportionally with the reaction temperature, reaching a maximum of 63% at 160 °C after 8 h of the reaction. In all cases, the FeNi-based catalysts appear to be completely selective towards the production of GVL (**3**), with only small traces (<1%) of 4-hydroxypentoic acid (**2**) observed. Then, by introducing the apparent kinetic constant obtained through magnetically induced catalysis (see SI section S9, Fig. S9.3) into the Arrhenius plot built upon the conventionally heated experiments (Fig. 5b), we were able to estimate the T_{surf} of **$Fe_1Ni_{0.25}$@N-G** during the magnetically induced hydrogenation of LA (Fig. 5d). The T_{surf} values of the MagNPs increase linearly over the entire range of the magnetic field, reaching a maximum T_{surf} of *ca.* 183 °C at 63 mT. These T_{surf} values were significantly higher than the T_{local} of the solution measured using an IR pyrometer, indicating a higher temperature at the catalyst surface. This result was expected since, in almost all cases, the conversions achieved at early reaction times through magnetic induction exceeded those obtained *via* conventional heating (Fig. 5d). For example, by comparing the results obtained at 100 °C under conventional heating (entry 2, Fig. 5c) with those obtained at 49 mT (T_{local}: 93 °C; see entry 3, Fig. 5d), it can be observed that the apparent kinetic constant is significantly higher in the case of the magnetically induced reaction ($k_{49\ mT}$: 0.151 min^{-1} *vs.* $k_{100\ °C}$: 0.125 min^{-1}). Similarly, when comparing the conversion results after 8 h, a conventional heated reaction conducted at 100 °C resulted in 33.4% conversion, whereas applying a magnetic field of 49 mT resulted in a higher conversion

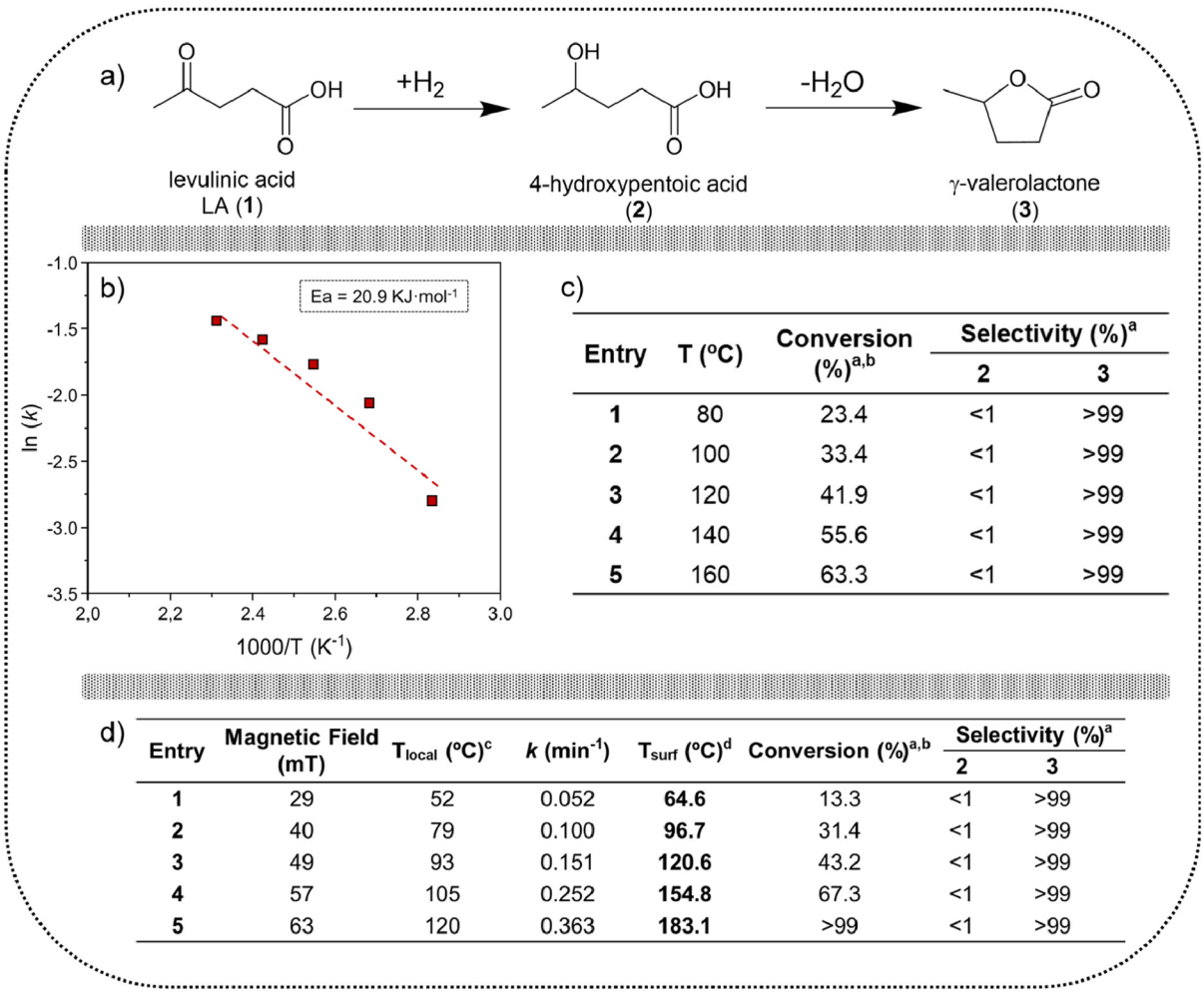

Entry	T (°C)	Conversion (%)[a,b]	Selectivity (%)[a]	
			2	3
1	80	23.4	<1	>99
2	100	33.4	<1	>99
3	120	41.9	<1	>99
4	140	55.6	<1	>99
5	160	63.3	<1	>99

d)

Entry	Magnetic Field (mT)	T_{local} (°C)[c]	k (min^{-1})	T_{surf} (°C)[d]	Conversion (%)[a,b]	Selectivity (%)[a]	
						2	3
1	29	52	0.052	**64.6**	13.3	<1	>99
2	40	79	0.100	**96.7**	31.4	<1	>99
3	49	93	0.151	**120.6**	43.2	<1	>99
4	57	105	0.252	**154.8**	67.3	<1	>99
5	63	120	0.363	**183.1**	>99	<1	>99

Fig. 5 (a) Schematic representation of LA hydrogenation. (b) Arrhenius plot of the conventionally heated conversion of LA into GVL using the **$Fe_1Ni_{0.25}$@N-G** catalyst. (c) Hydrogenation of LA catalysed by **$Fe_1Ni_{0.25}$@N-G** under conventional heating at different temperatures. (d) Determination of the T_{surf} during the magnetically induced hydrogenation of LA catalysed by **$Fe_1Ni_{0.25}$@N-G**. [a] Reaction conditions: 30 mg of **$Fe_1Ni_{0.25}$@N-G** (~9 mol% Ni), 0.4 mmol LA, 1 mL H_2O, and 5 bar H_2 for 8 h. Conversions and selectivities were determined by GC and GC-MS using dodecane as the internal standard, with carbon balances consistently in the 95–100% range. Product identities were further confirmed by NMR. [b] Blank test was performed in the hydrogenation of LA and the conversion was negligible. [c] T_{local} was measured using an IR pyrometer. [d] Estimated T_{surf} were calculated by the interpolation in the Arrhenius equation.

of 43.2%, although the measured T_{local} is slightly lower. This result suggests that the real temperature reached at the surface of the FeNi NPs is definitely higher than the one measured with the IR pyrometer, as evidenced after interpolation in the Arrhenius equation, which indicates a T_{surf} of 120 °C. Furthermore, by comparing the magnetically induced conversion of LA after 8 h at 49 mT (T_{surf}: *ca.* 120 °C) with the result obtained under conventional heating at 120 °C, we can observe that the conversions are almost identical, reaching 43.2% (entry 3, Fig. 5d) and 41.9% (entry 3, Fig. 5c) of LA conversion, respectively. The same trend can be observed when comparing the results obtained under conventional heating at 100 °C with those achieved by applying a magnetic field of 40 mT (T_{local}: 79 °C). Both catalytic reactions reach a very similar conversion value after 8 h, ~30% LA conversion, despite the significant temperature difference (see entry 2 Fig. 5c, and entry 2 Fig. 5d). As mentioned before, this phenomenon should occur because the T_{surf} of the catalyst in the reaction conducted at 40 mT is indeed higher than the T_{local} observed, with **$Fe_1Ni_{0.25}$@N-G** reaching a T_{surf} of *ca.* 97 °C at 40 mT.

In terms of energy efficiency, a comparison between magnetic induction heating and conventional heating using a hot plate (Heidolph, 0.825 kW) reveals a significant difference in energy savings. As previously mentioned, the main advantage of MIH lies in its rapid and direct heating of the catalyst itself, unlike conventional heating technologies that rely on external heat transfer. Firstly, when comparing the time required by both technologies to reach the target reaction temperature (T_{local} = 120 °C), the first difference becomes evident. Conventional heating requires approximately 19 min to reach the desired temperature, consuming around 262 W h, while MIH can achieve the same temperature in less than 1 minute, with a power consumption of only 34 W h. Therefore, during the heating ramp, MIH is nearly 8 times more energy-efficient than conventional heating. Secondly, when comparing the energy consumption required to reach the same conversion, further advantages of MIH become evident. For instance, to achieve a LA conversion of *ca.* 40% at T_{local} of 120 °C with **$Fe_1Ni_{0.25}$@N-G**, conventional heating requires 8 hours of reaction time, which implies a consumption of 6.6 kW h. In contrast, the same conversion can be achieved by MIH in only 2 hours, with a power input of less than 4 kW h. Furthermore, for nearly complete conversion of LA into GVL (96.2%) at 120 °C, conventional heating would require 22 hours, resulting in a total power demand of 18.2 kW h, whereas MIH reaches full conversion in just 8 hours, representing a significantly lower energy consumption (see SI section S9, Fig. S9.4).

As shown in Fig. 5d (entry 5), **$Fe_1Ni_{0.25}$@N-G** exhibits outstanding catalytic performance in the hydrogenation of LA, achieving complete conversion into GVL in water under 5 bar of H_2 at 63 mT, which corresponds to a T_{local} of 120 °C. Furthermore, no signs of size growth, agglomeration, or loss of the bimetallic character were observed by TEM and STEM-HAADF analysis (see SI section S4, Fig. S4.2 and S4.3), in contrast to what was observed in other studies where LA hydrogenation was addressed with FeNi-based nanoparticles.[14] We ascribe this behaviour to the fact that the FeNi NPs are well-encapsulated by the carbon layer and strongly interacting with the N atoms of the doped-support, providing the system with excellent stability.[65,73,74] Likewise, no significant reduction in BET surface area was observed after the magnetic catalytic reaction (see SI section S10, Fig. S10.1). Compared to the literature, magnetically heated **$Fe_1Ni_{0.25}$@N-G** stands out as one of the most active non-noble metal-based catalysts reported for the magnetically induced LA hydrogenation in aqueous media (see SI section S11, Table S11.1), under very mild catalytic conditions. To date, only two examples have been reported using water as the reaction medium for this transformation, and the TOF values in those studies are approximately one order of magnitude lower than the 1.3 h^{-1} achieved with **$Fe_1Ni_{0.25}$@N-G** (see entries 12–14 Table S11.1). This achievement is made possible by carrying out the reaction by magnetically induced heating, using equipment with only 2 kW of power. This enables LA hydrogenation at much lower temperatures and pressures than those typically reported in the literature (above 150 °C and 10–50 bar H_2), due to the formation of hot spots on the surface of the MagNPs where localized high temperatures and pressures are likely present.[11,75] In comparison, conventional heating methodologies require more severe conditions. For example, Balla *et al*. successfully converted LA into GVL using Ni NPs supported on carbon as the catalyst, but under high-temperature and high-pressure conditions (200 °C and 30 bar H_2).[50] Similarly, Kadu *et al*. synthesized FeNi-based NPs supported on montmorillonite (Ni/MMT), achieving a 41% conversion in aqueous media with complete selectivity toward GVL.[76] However, the reaction also required harsh conditions of 200 °C and 35 bar H_2, facing leaching issues after the first catalytic cycle.

To the best of our knowledge, very few studies have been reported in the literature on the magnetic induction hydrogenation of LA. In 2022, Gyergyek *et al*. were the first to report the use of magnetic induction for LA hydrogenation, with a Ru NP-based catalyst supported on maghemite.[51] Their results demonstrated excellent conversion and selectivity for GVL, using 2-propanol as solvent, 10 bar H_2, and a 6 kW magnetic induction system (see SI section S11, entry 11 Table S11.1). Due to the use of 2-propanol as solvent, Gyergyek and coworkers were able to achieve complete conversion into GVL with an energy consumption of only 600 W h, despite using magnetic equipment with a total power of 6 kW. This is partially attributed to the lower heat capacity of 2-propanol compared to water (2.68 J g^{-1} K^{-1} *vs.* 4.18 J g^{-1} K^{-1}, respectively), which allows the system to heat up with less energy input. Furthermore, when comparing the catalytic conditions used by Gyergyek with this work, it is worth noting that the solvent-to-catalyst mass ratio ($g_{solvent}/g_{catalyst}$) is three times lower in their case (23.3 *vs.* 66.7, respectively). Another limitation of their study was the use of noble metal nanoparticles, such as Ru, as the catalytically active species, which presents several disadvantages, including high cost due to limited availability. Overcoming this issue, later that same year, some of us developed a new heating agent based on non-noble metal NPs.

Specifically, Cerezo-Navarrete *et al*. reported using a carbon-based magnetic catalyst (FeCo@Ni@C) for the magnetically induced hydrogenation of biomass-derived molecules in an aqueous phase.[15] However, in that work, a very low conversion of LA into GVL was observed, achieving only 28.6% of conversion after 20 h of reaction using a 5 kW magnetic induction system (entry 12, Table S11.1). Some of us, also studied the hydrogenation of LA magnetically heated, achieving a maximum conversion of 73%, with no complete selectivity towards GVL, by using non-supported FeNi NPs stabilized with L-lysine and a high-power magnetic equipment of 13 kW (entry 13, Table S11.1).[14] Therefore, **$Fe_1Ni_{0.25}$@N-G** emerges as the most active magnetic catalyst based on Ni NPs reported to date for the magnetically induced hydrogenation of LA, achieving complete conversion into GVL using H_2O as solvent, 5 bar H_2, and a magnetic induction system of only 2 kW (entry 14, Table S11.1).

Motivated by the obtained results, we further evaluated the catalytic activity of **$Fe_1Ni_{0.25}$@N-G** in the hydrogenation of other oxygenated biomass-derived compounds, such as vanillin (**4**), levoglucosenone (**7**), and 5-hydroxymethylfurfural (HMF, **10**) in aqueous media (Table 2). For instance, the magnetically induced hydrogenation of vanillin (**7**) using **$Fe_1Ni_{0.25}$@N-G** resulted in a low conversion of 36.1% when a magnetic field of 40 mT was applied (see Table 2, entry 1). Nonetheless, it was fully selective to the formation of vanillyl alcohol (**5**). To achieve complete conversion with nearly full selectivity to vanillyl alcohol, it was necessary to extend the reaction time to 18 h under the same magnetic field (see Table 2, entry 2). However, by fixing the reaction time at 4 h and increasing the applied magnetic field, the conversion improved, and the selectivity shifted towards the hydrodeoxygenation (HDO) product, 2-methoxy-4-methylphenol (**6**). Indeed, a nearly complete conversion and selectivity to the HDO product was achieved upon applying a magnetic field of 63 mT. As shown in Table 2 (entries 2–4), the shift in selectivity towards the HDO product is attributed to the increased applied magnetic field, which raises the T_{local} reached during the reaction, as these parameters are directly correlated (see Fig. 5d). Specifically, at 40 mT, the **$Fe_1Ni_{0.25}$@N-G** catalyst reaches a T_{local} of 74 °C, which increases up to 130 °C when a magnetic field of 63 mT is applied. It is well known that hydrogenation reactions are favoured at lower temperatures, whereas HDO reactions are favoured at higher temperatures, explaining why the selectivity toward 2-methoxy-4-methylphenol becomes nearly complete at 63 mT.

A similar trend was observed in the hydrogenation of levoglucosenone (**7**), a product generated during cellulose pyrolysis, and recently established as a next-generation biomass-derived platform molecule.[77,78] Under a magnetic field of 40 mT, **$Fe_1Ni_{0.25}$@N-G** primarily produced dihydrolevoglucosenone (cyrene) (**8**), the product derived from the hydrogenation of the double bond. Specifically, after 2 h of reaction under a magnetic field of 40 mT, corresponding to a T_{local} of 72 °C, a conversion of 94% was achieved with 81% selectivity toward cyrene (**8**). However, increasing the applied magnetic field to

Table 2 Catalytic transformation of various biomass-derived compounds in aqueous media using **$Fe_1Ni_{0.25}$@N-G** as the magnetically active catalyst[a]

Entry	Substrates	Products	Field (mT)	Time (h)	T_{local}[b] (°C)	Conv.[c] (%)	Selectivity[c] (%)
1	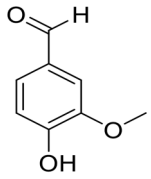	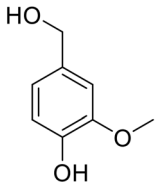 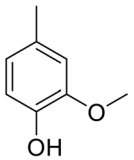	40	4	76	36.1	5 : 6 = 99 : 1
2			40	18	74	89.4	5 : 6 = 92 : 8
3			57	4	106	68.7	5 : 6 = 64 : 36
4			63	4	130	>99	5 : 6 = 3 : 97
	(4)	(5) (6)					
5	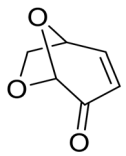	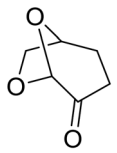 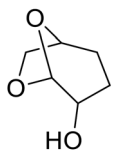	40	2	72	94.2	8 : 9 = 81 : 19
6			63	2	132	>99	8 : 9 = 12 : 88
7			63	4	132	>99	8 : 9 = 1 : 99
	(7)	(8) (9)					
8	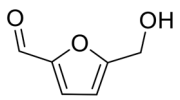	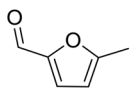 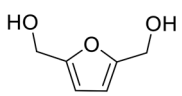	40	4	120	47.2	11 : 12 = 1 : 99
9			40	8	123	72.6	11 : 12 = 2 : 98
10			49	4	160	95.2	11 : 12 = 5 : 95
	(10)	(11) (12)					

[a] Reaction conditions: 30 mg of **$Fe_1Ni_{0.25}$@N-G** (~9 mol% Ni), 0.4 mmol substrate, 1 mL H_2O, and 5 bar H_2. [b] T_{local} was measured using an IR pyrometer. [c] Conversions and selectivities were determined by GC and GC-MS using dodecane as the internal standard, with carbon balances consistently in the 95–100% range. Product identities were further confirmed by NMR.

63 mT resulted in complete conversion within the same reaction time (2 h), but changing the selectivity to the product where the hydrogenation of the carbonyl (C=O) group was also achieved, reaching 88% selectivity for levoglucosanol (**9**) at a T_{local} of 132 °C (see Table 2, entry 6). Moreover, extending the reaction time from 2 to 4 h under the same conditions led to a quantitative yield of levoglucosanol (**9**) (see Table 2, entry 7).

Another molecule of great interest is HMF (**10**), a key biomass-derived platform chemical and an important building block for a wide range of applications in the field of polymers, fine chemicals, and fuels.[79–81] Similar to the other biomass-derived molecules, lower magnetic fields result in lower T_{local}, leading to poor conversion. For example, applying a magnetic field of 40 mT (T_{local} 120 °C) for 4 h results in a conversion of only 47.2% (see Table 2, entry 8) into 2,5-bishydroxymethylfuran (BHMF, **12**). Doubling the reaction time to 8 h under the same magnetic field (40 mT) increases the conversion to 72.6% (see Table 2, entry 9). Furthermore, increasing the magnetic field to 49 mT achieves an almost complete conversion of >95% (see Table 2, entry 10). Apparently, in the magnetically induced hydrogenation of HMF using **$Fe_1Ni_{0.25}$@N-G**, it was not possible to modulate product selectivity. This is due to the use of water as the reaction solvent, which usually drives the selectivity towards BHMF formation when using non-noble metal catalysts and low hydrogen pressures.[14,15]

Based on these results, it is worth noting that the hydrogenation of all biomass-derived products follows the same trend observed for levulinic acid: as the applied magnetic field increases, the T_{local} rises accordingly. However, the substrates clearly influence the T_{local} achieved, which is directly dependent on their heat capacity and density. For instance, under the same magnetic field of 40 mT, the observed T_{local} varies across the different substrates. While vanillin (**4**) and levoglucosenone (**7**) reach similar T_{local} of *ca.* 75 °C, HMF (**10**) achieves a significantly higher T_{local} of 120 °C (see Table 2, entries 1, 5, and 8). This is the reason why the hydrogenation of HMF was not carried out at a higher magnetic field (63 mT), as with the other substrates, since at such high temperatures (>150 °C), HMF tends to polymerize.[82]

Finally, a series of recycling experiments were performed to assess the robustness of the **$Fe_1Ni_{0.25}$@N-G** in the aqueous magnetic hydrogenation of LA. First, a reusability test was performed by repeatedly using the same batch of **$Fe_1Ni_{0.25}$@N-G** in the hydrogenation of LA at 63 mT for 4 h of reaction, ensuring that the comparison was not made under complete conversion conditions. Magnetic recoverability is another advantage of this system. Specifically, after each catalytic cycle of 4 h at 63 mT, the catalyst was separated using an external magnet, washed with H_2O and acetone, and dried in an oven at 100 °C. As shown in Fig. 6a, the first four consecutive catalytic cycles proceeded without any remarkable activity loss, maintaining a conversion close to 65%. However, from the fifth catalytic cycle onwards, a slight deactivation of the catalyst was observed, becoming more pronounced after the seventh cycle, with the conversion dropping to 17.2%. The catalyst deactivation can be attributed to a combination of different factors, including the partial oxidation of the MagNPs, and the metal leaching due to the highly acidic reaction conditions. According to Bai *et al.*, carrying out the hydrogenation of LA in aqueous media promotes the oxidation of the metal species, which, combined with the acidity of levulinic acid, leads to metal leaching through the formation of water-soluble complexes.[83] The partial oxidation of FeNi-based NPs could be observed by both XRD (see SI section S5, Fig. S5.2) and Raman spectroscopy (see SI section S7, Fig. S7.1f), where the vibrational bands associated with metal–oxygen bonds are detected. In the XRD analysis of the spent catalyst, the predominant contributions are associated with the partial oxidation of Fe (Fig. S5.2), mainly in the form of magnetite (Fe_3O_4). This finding was further confirmed by HRTEM analysis of the crystallographic planes of **$Fe_1Ni_{0.25}$@N-G** after the recycling experiments with LA, where lattice fringes with an interplanar distance of 2.48 Å were observed (see SI section S4, Fig. S4.4), corresponding to the (311) plane of *fcc*-Fe_3O_4 (JCPDS: 03-065-3107).

Magnetite is a less efficient heating agent than Fe^0, as evidenced by their Curie temperatures. While Fe^0 has a T_C of 770 °C, Fe_3O_4 exhibits a T_C of approximately 450–550 °C. As a result, **$Fe_1Ni_{0.25}$@N-G** becomes progressively less effective as a heating agent after each catalytic cycle due to its oxidation. This trend can be observed in Fig. 6a, where in the first catalytic cycle, the material reaches a T_{local} of 122 °C, but with each subsequent catalytic cycle, the temperature decreases, reaching only 77 °C in the seventh cycle. This decrease in the T_{local} achieved is due to the partial oxidation of the MagNPs, as can be observed through VSM and SAR measurements (see SI section S8, Fig. S8.6a). Partial oxidation is confirmed by the presence of an *exchange bias* in the hysteresis loops at 5 K after a field cooling in the presence of a $\mu_0 H$ of 3 T (see zoomed region in Fig. S8.6a), which is characteristic of the coupling between ferromagnetic and antiferromagnetic layers.[68] Consequently, this oxidation reduces the magnetic properties of **$Fe_1Ni_{0.25}$@N-G** (SAR_{before} = 50 W g^{-1} *vs.* SAR_{after} = 35 W g^{-1}) and, as a result, a decrease in the T_{local} achieved.

To verify whether the partial oxidation of the MagNPs was uniquely responsible for the decrease in conversion, the catalyst was subjected to reduction under H_2 (20 mL min^{-1}) at 300 °C for 2 h between the sixth and seventh cycles. This treatment led to a partial recovery of catalytic activity. From the seventh to the eighth cycle, the conversion increased from 17.2% to 48.4%, reaching a T_{local} of 108 °C (see Fig. 6a). These results confirm that the oxidation of MagNPs, primarily forming magnetite, is a limiting factor in the robustness of the catalyst. Furthermore, SAR measurements performed after the H_2 reduction pretreatment showed values analogous to those of the initial **$Fe_1Ni_{0.25}$@N-G** catalyst (see SI section S8, Fig. S8.7).

Nevertheless, the initial activity of **$Fe_1Ni_{0.25}$@N-G** does not fully recover after the reduction under H_2, suggesting that there is also catalyst deactivation possibly due to leaching caused by the acidity of LA in aqueous media (pK_a = 4.6).[84] As shown in Fig. 6a, catalyst leaching is negligible during the first

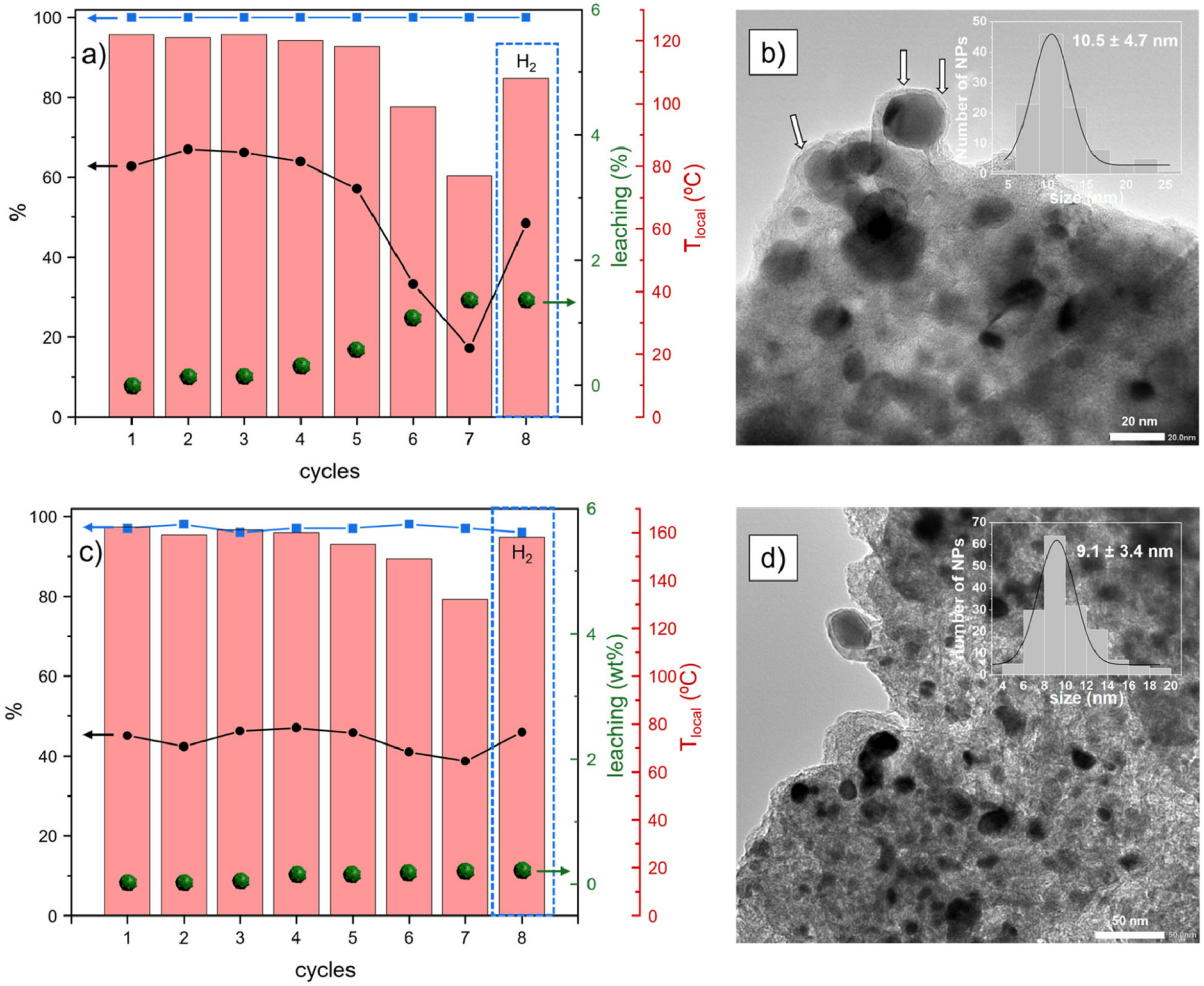

Fig. 6 Recycling experiments using **$Fe_1Ni_{0.25}$@N-G** with (a) LA and (c) HMF in aqueous media. Dashed lines indicate H_2 reduction pretreatment at 300 °C. Black dots and blue squares correspond to substrate conversion and product selectivity to GVL and BHMF, respectively (left axis), while green dots and red bars represent total metal leaching and local temperature (right axis). TEM and HRTEM images of **$Fe_1Ni_{0.25}$@N-G** after the reaction with (b) LA and (d) HMF, where the cracks of the carbon layer are highlighted by arrows. Reaction conditions: 30 mg of **$Fe_1Ni_{0.25}$@N-G** (~9 mol% Ni), 0.4 mmol of substrate, 1 mL of H_2O, and 5 bar H_2. T_{local} was measured using an IR pyrometer. Leaching studies were conducted using ICP-OES analysis.

catalytic cycles, consistently below 1 wt%. However, starting from the fifth cycle, a noticeable increase in leaching is observed, reaching a maximum of 4.9 wt% relative to the total catalyst mass. To confirm that leaching is exclusively due to the acidity of LA in the aqueous medium, we conducted the same recycling test, but using HMF (**10**) instead of LA. As can be observed in Fig. 6c, the **$Fe_1Ni_{0.25}$@N-G** catalyst seems to retain its initial activity over six consecutive catalytic cycles, maintaining a conversion of *ca.* 45% of HMF after 2 h of reaction at 49 mT, with selectivity towards BHMF exceeding 96% in all cases. However, in the seventh cycle, the conversion drops to 38.7%, suggesting catalyst deactivation. Therefore, we activated the **$Fe_1Ni_{0.25}$@N-G** in the same manner as we did for LA, by reducing the material under H_2 at 300 °C for 2 h. As a result, the conversion was fully recovered in the eighth cycle, reaching a value of 45.9%. Additionally, by examining the T_{local} achieved, we can observe a progressive decrease in the temperature, starting at 162 °C and decreasing to 132 °C in the seventh catalytic cycle. On the other hand, ICP-OES analysis shows only a minor leaching of the **$Fe_1Ni_{0.25}$@N-G**, never exceeding 0.25 wt% relative to the total mass of the catalyst. TEM and HRTEM micrographs also reveal the well encapsulation of the FeNi NPs, with a size distribution (9.1 ± 3.4 nm) similar to that of the as-synthesized catalyst (Fig. 6d), this result contrasts with the observations regarding **$Fe_1Ni_{0.25}$@N-G** after the recycling experiments with LA (Fig. 6b), where the MagNPs appear to be more aggregated, with a larger average size (10.5 ± 4.7 nm), due to the more acidic reaction conditions. Therefore, it is evident that the loss of catalytic activity in the stability studies of **$Fe_1Ni_{0.25}$@N-G** is due to a dual contribution: (i) the partial oxidation of the metal nanoparticles in water, which can be, at least partially recovered after H_2 reduction, and (ii) leaching caused by the acidic reaction conditions, only relevant in the reaction with LA.

It is evident that the superior catalytic activity of the bimetallic FeNi-based catalyst can be attributed to the incorporation of nickel into the Fe nanoparticles, as the **Fe@N-G** catalyst shows no activity in the magnetic hydrogenation of LA (see entry 1, Table S9.1). To investigate the promoting effect of nickel, we carried out a series of experiments. First, to estimate the accessible active surface sites of both **Fe@N-G** and **$Fe_1Ni_{0.25}$@N-G**, H_2 chemisorption measurements were performed. The H_2 uptake for **Fe@N-G** was 0.454 μmol g^{-1}, whereas for **$Fe_1Ni_{0.25}$@N-G**, it increased to 7.221 μmol g^{-1}. This enhancement confirms that the presence of nickel, forming FeNi bimetallic nanoparticles, increases hydrogen adsorption capacity due to the superior ability of Ni species to dissociate and activate molecular hydrogen efficiently.[72] The same trend observed in H_2-chemisorption experiments was further corroborated by comparing the activity of both catalysts (**Fe@N-G** and **$Fe_1Ni_{0.25}$@N-G**) in H/D exchange tests. As shown in Fig. S12.1 (see SI section S12), the HD signal was consistently higher for **$Fe_1Ni_{0.25}$@N-G** than for **Fe@N-G** across all tested temperatures (25, 60, and 90 °C), indicating a superior capacity of the bimetallic catalyst to dissociate hydrogen. These findings support the catalytic results observed (*vide supra*), where the monometallic Fe-based catalyst exhibited no activity, while the FeNi-based system showed clear activity in the magnetically induced hydrogenation of LA.

Second, temperature-programmed reduction (TPR) experiments were conducted to evaluate and compare the reducibility of **Fe@N-G**, **$Fe_1Ni_{0.1}$@N-G**, and **$Fe_1Ni_{0.25}$@N-G** catalysts (see SI section S13, Fig. S13.1). The TPR profile of **Fe@N-G** exhibited a main reduction peak at 287 °C, which shifted progressively to lower temperatures with increasing Ni content. In particular, the peak associated with the reduction of iron species in the bimetallic catalysts appeared at 281 °C for **$Fe_1Ni_{0.1}$@N-G** and at 275 °C for **$Fe_1Ni_{0.25}$@N-G** (see Fig. S13.1). This hydrogen consumption is attributed to the reduction of oxidized Fe species, identified by XPS analysis (see Fig. S6.2). On the other hand, nickel species were reduced at higher temperatures, and a similar trend was observed: the more nickel introduced into the system, the lower the Ni reduction temperature. Specifically, Ni reduction occurred at 367 °C for **$Fe_1Ni_{0.1}$@N-G** and at 352 °C for **$Fe_1Ni_{0.25}$@N-G**. These results clearly indicate that the presence of nickel facilitates the reduction of iron species, lowering the temperature required to fully reduce the catalyst. This improved reducibility may help explain why catalysts with higher Ni content exhibit increased SAR, which are associated with higher local temperatures under magnetic induction, ultimately leading to enhanced catalytic conversions.

Finally, adsorption of LA and GVL on the monometallic and bimetallic FeNi-based catalysts was investigated using high-performance liquid chromatography (HPLC) (see SI sections S1 and S14). **Fe@N-G** has a lower LA adsorption capacity than the bimetallic counterparts, **$Fe_1Ni_{0.1}$@N-G** and **$Fe_1Ni_{0.25}$@N-G**. While **Fe@N-G** only adsorbs 13.0 mg g_{cat}^{-1} of LA, **$Fe_1Ni_{0.1}$@N-G** and **$Fe_1Ni_{0.25}$@N-G** adsorb 27.2 and 33.6 mg g_{cat}^{-1}, respectively (see SI section S14, Fig. S14.1). However, the adsorption trend of the product GVL is the opposite. The monometallic **Fe@N-G** presents a higher adsorption capacity for GVL than **$Fe_1Ni_{0.1}$@N-G** and **$Fe_1Ni_{0.25}$@N-G** (17.7 mg g_{cat}^{-1} *vs.* 12.5 and 10.6 mg g_{cat}^{-1}, respectively). Therefore, this reveals that the bimetallic catalysts are capable of adsorbing LA more easily than **Fe@N-G**, but not GVL, which is in concordance with the magnetically induced catalytic results obtained (see SI section S9, Table S9.1). By comparing the LA/GVL adsorption ratios (Fig. S14.1), **$Fe_1Ni_{0.25}$@N-G** exhibits a much higher one ($A_{LA/GVL}$ = 3.2) than **$Fe_1Ni_{0.1}$@N-G** ($A_{LA/GVL}$ = 2.2), which could explain the superior catalytic activity observed by **$Fe_1Ni_{0.25}$@N-G**. These results evidence that the inclusion of nickel in the Fe NPs facilitates the adsorption of LA and weakens the adsorption of GVL, and explain the high selectivity of these bimetallic catalysts to the product of interest.

In conclusion, the incorporation of nickel enhances catalytic activity through multiple synergistic effects. Ni promotes H_2 activation, as evidenced by the significant increase in hydrogen uptake and enhanced H/D exchange. It also facilitates the reduction of Fe and Ni species, lowering the reduction temperatures and improving catalyst activation under reaction conditions. Additionally, Ni modifies the surface adsorption properties, increasing the uptake of LA while suppressing GVL adsorption, which aligns with the observed improvements in conversion and selectivity. All in all, these combined effects rationalize the superior performance of the Ni-containing catalysts.

Conclusions

In this work, we present a green, scalable, and cost-effective synthetic strategy for the preparation of FeNi-based MagNPs encapsulated in N-doped graphitic carbon through a single-step pyrolysis of glucose, a renewable carbon source. A series of five different magnetic catalysts with varying Fe/Ni atomic ratios were synthesized: **Fe@N-G**, **$Fe_1Ni_{0.05}$@N-G**, **$Fe_1Ni_{0.1}$@N-G**, **$Fe_1Ni_{0.25}$@N-G**, and **$Fe_1Ni_{0.4}$@N-G**. These bimetallic FeNi-based catalysts serve simultaneously as efficient heating agents under an alternating magnetic field and as active catalysts for the hydrogenation of biomass-derived substrates in aqueous media.

Among the synthesized compositions, **$Fe_1Ni_{0.25}$@N-G** demonstrated the most promising catalytic behavior, exhibiting complete conversion of LA with a 100% selectivity toward GVL under mild conditions (5 bar H_2 and T_{local} 120 °C) using a moderate magnetic field (63 mT, 320 kHz, 2 kW). Notably, **$Fe_1Ni_{0.25}$@N-G** emerges as the most active Ni-based magnetic catalyst reported to date for the MIH hydrogenation of LA in aqueous media, even using a relatively low power equipment (2 kW). Importantly, MIH was shown to be approximately eight times more energy-efficient than conventional heating, representing a significant step toward more sustainable catalytic processes. Furthermore, the catalyst also showed high activity and selectivity in the hydrogenation of other relevant biomass-derived molecules such as levoglucosenone, vanillin, and HMF, further demonstrating its versatility.

The encapsulation of FeNi NPs within a N-doped graphitic carbon matrix significantly improved both catalytic performance and structural stability compared to similar previous studies in water, preventing the growth of the MagNPs. Although partial deactivation was observed after four cycles in LA hydrogenation owing to oxidation and metal leaching, due to the acidic aqueous conditions (pH ~2), a simple H_2-reduction treatment partially restored the catalytic activity. In contrast, the catalyst maintained full activity across eight cycles when applied to the hydrogenation of HMF, highlighting its robustness when used under neutral conditions.

Overall, this study showcases the potential of magnetic induction heating as a sustainable and efficient technology for catalytic biomass valorization and reinforces the promise of using alternative approaches for synthesizing MagNPs (**Fe_1Ni_x@N-G**), which are reusable, bifunctional materials, tailored for green chemical transformations.

Conflicts of interest

There are no conflicts to declare.

Data availability

All data supporting this article, including detailed experimental procedures, characterization techniques (such as XRD, TEM, XPS, and BET analysis), and additional catalytic results that supports the findings, have been included in the SI. See DOI: **https://doi.org/10.1039/d5gc03853g**.

Additionally, unformatted raw data are available from the authors upon request.

Acknowledgements

The authors are thankful for the financial support from the European Union's Horizon 2020 research and innovation program under grant agreement no. 101022507. Financial support from the Severo Ochoa Centre of Excellence Program (CEX2021-001230-S) is gratefully acknowledged. In addition, this work has received funding from the Spanish Government (PID2022-140111OB-I00 and TED2021-130191B-C41 funded by MCIN/AEI/ 10.13039/501100011033 and European Union NextGenerationEU/PRTR). This study forms a part of the Advanced Materials program and was supported by MCIN with partial funding from European Union Next Generation EU (PRTR-C17. I1) and by Generalitat Valenciana (MFA/2022/047). J. M. acknowledges his MSCA individual postdoctoral fellowship from the Horizon Europe research and innovation program (Project 101109254-BIOCATMAG) for funding. The authors thank Instituto de Tecnología Química (ITQ), Consejo Superior de Investigaciones Científicas (CSIC) and Universitat Politècnica de València (UPV) for the facilities. We also thank the UPV Electron Microscopy Service for the TEM analysis and Magnetic Measurements Service of LPCNO.

References

1 W. Wang, G. Tuci, C. Duong-Viet, Y. Liu, A. Rossin, L. Luconi, J. M. Nhut, L. Nguyen-Dinh, C. Pham-Huu and G. Giambastiani, *ACS Catal.*, 2019, **9**, 7921–7935.
2 L. Truong-Phuoc, C. Duong-Viet, J. M. Nhut, A. Pappa, S. Zafeiratos and C. Pham-Huu, *ChemSusChem*, 2025, e202402335.
3 J. Marbaix, N. Mille, J. Carrey, K. Soulantica and B. Chaudret, in *Nanoparticles in Catalysis*, ed. K. Philippot and A. Roucoux, Wiley, 2021, pp. 307–329.
4 J. S. Pavelić, S. Gyergyek, B. Likozar and M. Grilc, *Chem. Eng. J.*, 2025, **505**, 158928.
5 C. Hu, Y. Dong, Q. Shi, R. Long and Y. Xiong, *Chem. Soc. Rev.*, 2025, **54**, 524–559.
6 A. García-Zaragoza, J. L. del Río-Rodríguez, C. Cerezo-Navarrete, S. Gutiérrez-Tarriño, M. A. Molina, L. Costley-Wood, J. Mazarío, B. Chaudret, L. M. Martínez-Prieto, A. M. Beale and P. Oña-Burgos, *ACS Catal.*, 2025, 9489–9502.
7 S. Ceylan, C. Friese, C. Lammel, K. Mazac and A. Kirschning, *Angew. Chem., Int. Ed.*, 2008, **47**, 8950–8953.
8 T. K. Houlding and E. V. Rebrov, *Green Process. Synth.*, 2012, **1**, 19–31.
9 C. Cerezo-Navarrete, I. M. Marin, C. Marini, B. Chaudret and L. M. Martínez-Prieto, *Appl. Catal., B*, 2024, **347**, 123780.
10 M. N. Pérez-Camacho, J. Abu-Dahrieh, D. Rooney and K. Sun, *Catal. Today*, 2015, **242**, 129–138.
11 J. M. Asensio, J. Marbaix, N. Mille, L. M. Lacroix, K. Soulantica, P. F. Fazzini, J. Carrey and B. Chaudret, *Nanoscale*, 2019, **11**, 5402–5411.
12 S. Gyergyek, A. Kocjan, M. Grilc, B. Likozar, B. Hočevar and D. Makovec, *Green Chem.*, 2020, **22**, 5978–5983.
13 Z. J. Díaz-Puerto, Á. Raya-Barón, P. W. N. M. Van Leeuwen, J. M. Asensio and B. Chaudret, *Nanoscale*, 2021, **13**, 12438–12442.
14 Á. Raya-Barón, J. Mazarío, G. Mencia, P. F. Fazzini and B. Chaudret, *ChemSusChem*, 2023, **16**, e202300009.
15 C. Cerezo-Navarrete, I. M. Marin, H. García-Miquel, A. Corma, B. Chaudret and L. M. Martínez-Prieto, *ACS Catal.*, 2022, **12**, 8462–8475.
16 J. Mazarío, V. Varela-Izquierdo and B. Chaudret, in *Topics in Organometallic Chemistry*, Springer Science and Business Media Deutschland GmbH, 2024, vol. 75, pp. 243–271.
17 E. G. Acheson, *US Patent*, 568323, 1896.
18 R. D. Hunter, J. Ramírez-Rico and Z. Schnepp, *J. Mater. Chem. A*, 2022, **10**, 4489–4516.
19 A. Gomez-Martin, J. Martinez-Fernandez, M. Ruttert, A. Heckmann, M. Winter, T. Placke and J. Ramirez-Rico, *ChemSusChem*, 2018, **11**, 2776–2787.
20 C. Zhang, Z. Wu, S. Jan, Z. Wang, S. Bennaceur, H. K. Kim and X. Jin, *Electrochim. Acta*, 2021, **390**, 138800.
21 S. Lyu, L. Wang, Z. Li, S. Yin, J. Chen, Y. Zhang, J. Li and Y. Wang, *Nat. Commun.*, 2020, **11**, 1–8.
22 H. Niu, Y. Wang, X. Zhang, Z. Meng and Y. Cai, *ACS Appl. Mater. Interfaces*, 2012, **4**, 286–295.

23 C. Defilippi, M. O. A. Mukadam, S. A. Nicolae, M. R. Lees and C. Giordano, *Materials*, 2019, **12**, 323.
24 R. D. Hunter, J. L. Rowlandson, G. J. Smales, B. R. Pauw, V. P. Ting, A. Kulak and Z. Schnepp, *Mater. Adv.*, 2020, **1**, 3281–3291.
25 S. Gyergyek, E. Chernyshova, K. Böőr, M. Nečemer and D. Makovec, *J. Alloys Compd.*, 2023, **953**, 170139.
26 M. Besson, P. Gallezot and C. Pinel, *Chem. Rev.*, 2014, **114**, 1827–1870.
27 J. Pritchard, G. A. Filonenko, R. Van Putten, E. J. M. Hensen and E. A. Pidko, *Chem. Soc. Rev.*, 2015, **44**, 3808–3833.
28 L. Zhang, T. U. Rao, J. Wang, D. Ren, S. Sirisommboonchai, C. Choi, H. Machida, Z. Huo and K. Norinaga, *Fuel Process. Technol.*, 2022, **226**, 107097.
29 F. D. Pileidis and M. M. Titirici, *ChemSusChem*, 2016, **9**, 562–582.
30 D. M. Alonso, S. H. Hakim, S. Zhou, W. Won, O. Hosseinaei, J. Tao, V. Garcia-Negron, A. H. Motagamwala, M. A. Mellmer, K. Huang, C. J. Houtman, N. Labbé, D. P. Harper, C. T. Maravelias, T. Runge and J. A. Dumesic, *Sci. Adv.*, 2017, **3**, e1603301.
31 L. Karam and C. N. Neumann, *ChemCatChem*, 2022, **14**, e202200953.
32 I. T. Horváth, H. Mehdi, V. Fábos, L. Boda and L. T. Mika, *Green Chem.*, 2008, **10**, 238–242.
33 K. Yan, Y. Yang, J. Chai and Y. Lu, *Appl. Catal., B*, 2015, **179**, 292–304.
34 J. Molleti, M. S. Tiwari and G. D. Yadav, *Chem. Eng. J.*, 2018, **334**, 2488–2499.
35 X. Du, Y. Liu, J. Wang, Y. Cao and K. Fan, *Chin. J. Catal.*, 2013, **34**, 993–1001.
36 A. S. Amarasekara and M. A. Hasan, *Catal. Commun.*, 2015, **60**, 5–7.
37 J. N. Putro, A. Kurniawan, F. E. Soetaredjo, S. Y. Lin, Y. H. Ju and S. Ismadji, *RSC Adv.*, 2015, **5**, 41285–41299.
38 D. J. Braden, C. A. Henao, J. Heltzel, C. C. Maravelias and J. A. Dumesic, *Green Chem.*, 2011, **13**, 1755–1765.
39 S. G. Wettstein, J. Q. Bond, D. M. Alonso, H. N. Pham, A. K. Datye and J. A. Dumesic, *Appl. Catal., B*, 2012, **117–118**, 321–329.
40 Z. P. Yan, L. Lin and S. Liu, *Energy Fuels*, 2009, **23**, 3853–3858.
41 O. A. Abdelrahman, A. Heyden and J. Q. Bond, *ACS Catal.*, 2014, **4**, 1171–1181.
42 Q. Guan, H. Li, H. Wen, Z. Qiu and Y. Cao, *Catal. Lett.*, 2024, **154**, 4864–4872.
43 A. M. Hengne and C. V. Rode, *Green Chem.*, 2012, **14**, 1064–1072.
44 S. S. R. Gupta and M. L. Kantam, *Catal. Today*, 2018, **309**, 189–194.
45 A. García, R. Sanchis, P. J. Miguel, A. M. Dejoz, M. P. Pico, M. L. López, I. Álvarez-Serrano, T. García and B. Solsona, *RSC Adv.*, 2020, **10**, 20395–20404.
46 Y. R. Shao, L. Zhou, L. Yu, Z. F. Li, Y. T. Li, W. Li and T. L. Hu, *ACS Appl. Mater. Interfaces*, 2022, **14**, 17195–17207.
47 A. Chauhan, R. Bal and R. Srivastava, *Energy Fuels*, 2024, **38**, 5998–6011.
48 R. Kuna, P. Balla, N. P. Rajan, B. Ponnala, S. Hussain and V. R. C. Komandur, *React. Kinet., Mech. Catal.*, 2022, **135**, 183–199.
49 H. Xu, D. Hu, Z. Yi, Z. Wu, M. Zhang and K. Yan, *ACS Appl. Energy Mater.*, 2019, **2**, 6979–6983.
50 P. Balla, P. K. Seelam, R. Balaga, R. Rajesh, V. Perupogu and T. X. Liang, *J. Environ. Chem. Eng.*, 2021, **9**, 106530.
51 S. Gyergyek, M. Grilc, B. Likozar and D. Makovec, *Green Chem.*, 2022, **24**, 2788–2794.
52 S. Brunauer, P. H. Emmett and E. Teller, *J. Am. Chem. Soc.*, 1938, **60**, 309–319.
53 E. P. Barrett, L. G. Joyner and P. P. Halenda, *J. Am. Chem. Soc.*, 1951, **73**, 373–380.
54 C. Cerezo-Navarrete, Y. Mathieu, M. Puche, C. Morales, P. Concepción, L. M. Martínez-Prieto and A. Corma, *Catal. Sci. Technol.*, 2021, **11**, 494–505.
55 J. S. Martinez, J. Mazarío, C. W. Lopes, S. Trasobares, J. J. Calvino Gamez, G. Agostini and P. Oña-Burgos, *ACS Catal.*, 2024, **14**, 4768–4785.
56 B. Moeini, M. R. Linford, N. Fairley, A. Barlow, P. Cumpson, D. Morgan, V. Fernandez and J. Baltrusaitis, *Surf. Interface Anal.*, 2022, **54**, 67–77.
57 M. Ayiania, M. Smith, A. J. R. Hensley, L. Scudiero, J. S. McEwen and M. Garcia-Perez, *Carbon*, 2020, **162**, 528–544.
58 D. J. Morgan, *C*, 2021, **7**, 51.
59 Y. Yamada, J. Kim, S. Matsuo and S. Sato, *Carbon*, 2014, **70**, 59–74.
60 K. Artyushkova, *J. Vac. Sci. Technol., A*, 2020, **38**, 31002.
61 M. C. Biesinger, B. P. Payne, L. W. M. Lau, A. Gerson and R. S. C. Smart, *Surf. Interface Anal.*, 2009, **41**, 324–332.
62 M. C. Biesinger, B. P. Payne, A. P. Grosvenor, L. W. M. Lau, A. R. Gerson and R. S. C. Smart, *Appl. Surf. Sci.*, 2011, **257**, 2717–2730.
63 X. Liu, X. Li, Y. Sun, S. Zhang and Y. Wu, *Appl. Surf. Sci.*, 2019, **479**, 318–325.
64 R. Saito, M. Hofmann, G. Dresselhaus, A. Jorio and M. S. Dresselhaus, *Adv. Phys.*, 2011, **60**, 413–550.
65 L. M. Martínez-Prieto, M. Puche, C. Cerezo-Navarrete and B. Chaudret, *J. Catal.*, 2019, **377**, 429–437.
66 S. P. Gubin, *Magnetic Nanoparticles*, John Wiley and Sons, 2009.
67 M. Y. Lavrentiev, J. S. Wróbel, D. Nguyen-Manh and S. L. Dudarev, *Phys. Chem. Chem. Phys.*, 2014, **16**, 16049–16059.
68 J. Nogués and I. K. Schuller, *J. Magn. Magn. Mater.*, 1999, **192**, 203–232.
69 J. Q. Bond, D. M. Alonso, D. Wang, R. M. West and J. A. Dumesic, *Science*, 2010, **327**, 1110–1114.
70 F. Valentini, G. Brufani, B. Di Erasmo and L. Vaccaro, *Curr. Opin. Green Sustainable Chem.*, 2022, **36**, 100634.
71 T. Kitanosono, K. Masuda, P. Xu and S. Kobayashi, *Chem. Rev.*, 2018, **118**, 679–746.
72 X. Yu and C. T. Williams, *Catal. Sci. Technol.*, 2023, **13**, 802–825.

73 R. V. Siva Prasanna Sanka, K. Balaji, Y. Leterrier, S. Pandey, M. Srivastava, A. Srivastava, W. H. Binder, S. Rana and V. Michaud, *Chem. Commun.*, 2019, **55**, 6249–6252.
74 J. H. Advani, N. U. H. Khan, H. C. Bajaj and A. V. Biradar, *Appl. Surf. Sci.*, 2019, **487**, 1307–1315.
75 J. M. Asensio, A. B. Miguel, P. Fazzini, P. W. N. M. van Leeuwen and B. Chaudret, *Angew. Chem., Int. Ed.*, 2019, **58**, 11306–11310.
76 B. S. Kadu, A. M. Hengne, N. S. Biradar, C. V. Rode and R. C. Chikate, *Ind. Eng. Chem. Res.*, 2016, **55**, 13032–13039.
77 S. H. Krishna, D. J. McClelland, Q. A. Rashke, J. A. Dumesic and G. W. Huber, *Green Chem.*, 2017, **19**, 1278–1285.
78 J. Mazarío, M. Parreño Romero, P. Concepción, M. Chávez-Sifontes, R. A. Spanevello, M. B. Comba, A. G. Suárez and M. E. Domine, *Green Chem.*, 2019, **21**, 4769–4785.
79 R. J. Van Putten, J. C. Van Der Waal, E. De Jong, C. B. Rasrendra, H. J. Heeres and J. G. De Vries, *Chem. Rev.*, 2013, **113**, 1499–1597.
80 J. Zhang, D. N. Li, H. R. Yuan, S. R. Wang and Y. Chen, *J. Fuel Chem. Technol.*, 2021, **49**, 1752–1766.
81 W. Fang and A. Riisager, *Green Chem.*, 2021, **23**, 670–688.
82 G. Tsilomelekis, M. J. Orella, Z. Lin, Z. Cheng, W. Zheng, V. Nikolakis and D. G. Vlachos, *Green Chem.*, 2016, **18**, 1983–1993.
83 X. Bai, T. Ren, J. Mao, S. Li, J. Yin and J. Zhou, *New J. Chem.*, 2020, **44**, 16526–16536.
84 K. Yan, C. Jarvis, J. Gu and Y. Yan, *Renewable Sustainable Energy Rev.*, 2015, **51**, 986–997.